1 **Micromechanics of Undrained Response of Dilative Granular Media**

2 **Using a Coupled DEM-LBM Model: A Case of Biaxial Test**

3

4 Daniel H. Johnson[1], Farshid Vahedifard[2], Bohumir Jelinek[3], John F. Peters[4]

5 [1] Graduate Student, Dept. of Mechanical Engineering and Center for Advanced Vehicular Systems
6 (CAVS), Mississippi State University, Mississippi State, MS 39762, USA. email:
7 dhj21@cavs.msstate.edu

8 [2] Corresponding Author, Assistant Professor, Dept. of Civil and Environmental Engineering and
9 Center for Advanced Vehicular Systems (CAVS), Mississippi State University, Mississippi State,
10 MS 39762, USA. email: farshid@cee.msstate.edu

11 [3] Assistant Research Professor, Center for Advanced Vehicular Systems (CAVS), Mississippi State
12 University, Mississippi State , MS 39762, USA, email: bj48@cavs.msstate.edu

13 [4] Associate Research Professor, Center for Advanced Vehicular Systems (CAVS), Mississippi
14 State University, Mississippi State , MS 39762, USA, email: particledad@gmail.com

15

16 **Abstract**

17 In this paper the Discrete Element Method (DEM) is coupled with the Lattice-Boltzmann

18 Method (LBM) to model the undrained condition of dense granular media that display significant

19 dilation under highly confined loading. DEM-only models are commonly used to simulate the

20 micromechanics of an undrained specimen by applying displacements at the domain boundaries

21 so that the specimen volume remains constant. While this approach works well for uniform strain

22 conditions found in laboratory tests, it doesn't realistically represent non-uniform strain conditions

23 that exist in the majority of real geotechnical problems. The LBM offers a more realistic approach

24 to simulate the undrained condition since the fluid can locally conserve the system volume. To

25 investigate the ability of the DEM-LBM model to effectively represent the undrained constraint

26 while conserving volume and accurately calculating the stress path of the system, a two

27   dimensional biaxial test is simulated using the coupled DEM-LBM model, and the results are

28   compared with those attained from a DEM-only constant volume simulation. The compressibility

29   of the LBM fluid was found to play an important role in the model response. The compressibility

30   of the fluid is expressed as an apparent Skempton's pore pressure parameter B. The biaxial test,

31   both with and without fluid, demonstrated particle-scale instabilities associated with shear band

32   development. The results show that the DEM-LBM model offers a promising technique for a

33   variety of geomechanical problems that involve particle-fluid mixtures undergoing large

34   deformation under shear loading.

35

36   **Keywords:** Discrete Element Method; Lattice-Boltzmann Method; Undrained Loading;

37   Dilatancy; Skempton's Pore Pressure Parameter; Micromechanics

38   **1. Introduction**

39   The interaction of solid and water phases in granular media is central to the science and

40   practice of soil mechanics [1]. Mathematically, this interaction is described by coupling the partial

41   differential equations of deformation and fluid flow to produce a system that can model the

42   deformation of soil-water mixtures starting from an initial "undrained" loading, going through the

43   process of consolidation, resulting in a final "drained" state. Such a complex physical system can

44   be modeled by coupling two simpler components due to the effective stress principle, which

45   decomposes the applied total stress into additive components acting separately on the fluid and

46   solid phases [2].

47   An accurate representation of the constitutive relationship for soil remains the key issue in

48   geotechnical modeling despite a nearly half-century of intensive research. The most difficult

49   problems are those involving large discontinuous deformations as encountered in failures (e.g.,

50　landslides, liquefaction) or erosional failures associated with internal erosion and piping. The

51　Discrete Element Method (DEM), originally developed by Cundall and Stack [3], offers a

52　fundamental approach to modeling granular materials at the particle scale. The DEM has the

53　advantage of modeling the motion of individual grains, thus naturally capturing large

54　discontinuous deformations that confound continuum formulations. The Lattice-Boltzmann

55　method (LBM) is a natural companion to the DEM for modeling the fluid phase because both are

56　based on explicit time integration and simple spatial discretization, whereby the simple lattice of

57　the LBM fits well with the cubical grid generally used to localize neighbor searches in the DEM

58　[4]. The DEM has been used extensively to study localization phenomena in granular media [5]

59　with recent studies including the evolution of fluid flow [6]. Coupled DEM-LBM modeling has

60　likewise been applied to piping problems [7]. A comprehensive overview of applying the DEM

61　and LBM in these multi-scale problems can be found in [4].

62　　　Previous studies have used coupled DEM-LBM models mainly for cases where the soil

63　grains are in a relatively unconfined condition such as sedimentation, fluidized beds, liquefaction

64　phenomena, and piping [4-5, 7]. This study focuses on an undrained test that involves highly

65　confined loading between rigid platens of dense particle systems displaying significant dilation, a

66　case which has not been examined in the previous DEM-LBM modeling efforts. The term

67　"confined" emphasizes the contrast to cases where the particles have a high degree of free motion

68　such as in simulations of fluidized beds and liquefaction. In essence, the particles are confined

69　because they must deform within the constraints of the four loading platens. Herein, a biaxial

70　loading case is chosen to investigate the suitability of the DEM-LBM for modeling the undrained

71　condition in dilative granular media. Biaxial loading is a two dimensional approximation to

72　standard laboratory tests such as the triaxial, cubical triaxial, and plane strain tests and is

3

73 commonly used to address general academic questions involving granular media physics and the

74 numerical aspects of the DEM. Recently, several studies have been performed on using the DEM

75 to simulate the biaxial case with the undrained condition and to better understand the effects of

76 important DEM parameters (e.g., [8-10]). It is common to impose the constant-volume condition

77 in the DEM only models by applying displacements at the domain boundaries such that the

78 specimen volume remains constant. Although this approach works well for uniform strain

79 conditions found in laboratory tests, it is not practical for study of general geotechnical problems

80 such as slope stability, which pose non-uniform strain conditions. To address this gap this study

81 uses the LBM to capture the response of fluid undergoing a compressive load. This provides a

82 more realistic approach to extending undrained models to conditions of non-uniform strain because

83 the fluid *locally* conserves system volume in the LBM.

84   Following this introductory section, the paper provides brief descriptions of the DEM and

85 LBM including their coupling, with a discussion on time integration and spatial resolution of each

86 method. This section is followed by a description of the biaxial test and the instability associated

87 with shear localization as documented in several previous publications [11-13]. Finally, an

88 investigation of the effects of fluid compressibility and particle sizes on the results is presented.

2. Numerical Method

90   In recent years, coupling the DEM with LBM has become a well-established method for

91 solving fluid-particle interaction problems in geomechanics [1, 6-7, 12]. In this coupled method,

92 the DEM resolves the inter-particle interactions, and the LBM solves the Navier-Stokes equations

93 for the fluid flow. Also, although not considered in the present study, the coupled DEM-LBM has

94 the potential to model the relative motion of soil grains and water found in consolidation problems.

95 Feng et al. [14] used the DEM-LBM to model a vacuum dredging system for mineral recovery,

96   where particles are pulled through a suction pipe at turbulent Reynolds numbers. Lomine et al. [7]

97   used the DEM-LBM to model piping erosion. In these simulations, 2D discs were placed in a

98   rectangular domain, and a pressure gradient was applied to drive the fluid flow. The DEM-LBM

99   coupling is advantageous because both methods employ explicit time integration making them

100   particularly suitable for parallelization [15].

101   The following sections briefly discuss the DEM and LBM formulations, boundary

102   conditions, and coupling between the DEM and LBM applied in this study.

103   *2.1. Discrete Element Method*

104   The DEM is a procedure for simulating interacting bodies through integration of the

105   equations of motion for each body. The contact forces are calculated using binary contact laws

106   based on the relative displacement of the bodies at the point of their contact. Thus the bodies

107   themselves are assumed rigid. DEM is designed to simulate granular media in large assemblages,

108   ranging from a few thousand particles to millions of particles. To simplify contact detection,

109   particles are often assumed to be spherical, but not necessarily of equal size. Spherical particles

110   are used as a computational expedient; non-spherical particles can be modeled, although at the

111   expense of added memory usage to describe particle geometry and added computational time for

112   contact detection.

113   Interactions between particles are described by contact laws that define forces and

114   moments created by relative motions of the particles. The particle acceleration is computed from

115   the summation of contact forces acting on each particle combined with external forces. The motion

116   of each particle that results from the net forces and moments are obtained by integrating Newton's

117   laws. Thus, the particles are not treated as a continuous medium. Rather, the medium behavior

118   emerges from the interactions of the particles comprising the assemblage [3].

119   The evolution of particle velocity, v_i and rotational rate ω_i are given by

$$m\frac{\partial v_i}{\partial t} = mgn_i^g + \sum_{c=1}^{N_c} f_i^c + F_F \tag{1}$$

120   and

$$I_m\rho\,\frac{\partial \omega_i}{\partial t} = \sum_{c=1}^{N_c} e_{ijk}f_j^c r_k^c + \sum_{c=1}^{N_c} M_i^c + T_F \tag{2}$$

121   where m and I_m are the particle mass and moment of inertia respectively, gn_i^g the acceleration of

122   gravity, f_i^c and M_i^c the forces and moments applied at the contacts, F_F and T_F are the hydrodynamic

123   force and torque, respectively, and N_c the number of contacts for the particle.

124   Particle forces are accumulated from pairwise interactions between particles. Two particles

125   with radii R_A and R_B make contact when the distance, d, separating the particles satisfies

$$d < R_A + R_B. \tag{3}$$

126   The contact forces and moments arise from relative motion between contacting particles.

127   The motion of each individual particle is described by the velocity of the particle center and the

128   rotation about the center. The branch vector between particle centers, $x_i^A - x_i^B$ is also the difference

129   between the respective radii vectors that link the particle centers to the contact $r_i^A - r_i^B$. With this

130   nomenclature, the relative motion at contact c between particles A and B is given by

$$\Delta_i^c = u_i^A - u_i^B + e_{ijk}\left(r_j^A \theta_k^A - r_j^B \theta_k^B\right). \tag{4}$$

131   where repeated indices indicates summation. The contact moments are generated by the difference

132   in rotations, $\Delta\omega_i^c$, between the particles,

$$\Delta\omega_i^c = \omega_i^A - \omega_i^B. \tag{5}$$

133   The contact forces for cohesionless materials are given by the contact laws in terms of their

134   normal and shear components, f^n, and f_i^s

$$f^n = \begin{cases} K^n \Delta^n \\ E_r K^n (\Delta^o - \Delta^n), \end{cases} \qquad \Delta^n < \Delta^o, \tag{6}$$

$$f_i^s = \begin{cases} K^s \Delta_i^s \\ f^n \tan \phi\, n_i^s, \end{cases} \qquad |f_i^s| \geq f^n \tan \phi, \tag{7}$$

$$m_i^c = \begin{cases} K^m \Delta \omega_i^c \\ f^n \tan \phi_m\, n_i^m, \end{cases} \qquad |m_i^c| \geq f^n \tan \phi_m, \tag{8}$$

135   where K^n and K^s are stiffness constants; E_r is a factor to dissipate energy through stiffening the

136   unload response; Δ^n and Δ_i^s are the normal and shear components of the contact displacement; n_i^s

137   and n_i^m are the unit vectors in the direction of the shear force and moment; Δ^o is the greatest value

138   of penetration in the history of Δ^n; and ϕ and ϕ_m are friction parameters.

139   Following Peters *et al.* (2005), the particle stress tensor and the average continuum stress

140   in the solid fraction are defined as:

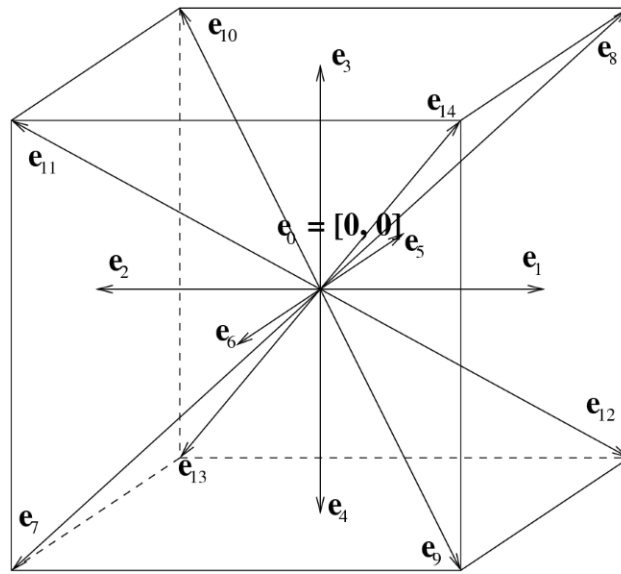$$\sigma_{ij}^p = \frac{1}{V_p} \sum_{c=1}^{N^c} f_i^c r_j^c \tag{9}$$

$$\bar{\sigma}_{ij} = \frac{1}{V} \sum_{p=1}^{N^p} V_p \sigma_{ij}^p = \frac{V_s}{V} \langle \sigma_{ij}^p \rangle \tag{10}$$

141   where V is the total volume, V_p is the volume of each particle, V_s is the total particle volume, N^c is

142   the number of contacts, N^p is the number of particles, f_i^c is the ith component of the force acting at

143   the contact, r_j^c is the jth component of the radius vector from the center of the particle to the contact.

144   The particle stresses identify the particles transmitting higher than average loads through force

145   chains. The average continuum stress is calculated to investigate the stress history of the system

146   in the form of a stress path plot of the intergranular stress, p, and the deviatoric stress, q.

147

148   *2.2. Lattice Boltzmann Method*

149   The LBM is a simulation technique commonly used for solving fluid flow and transport

150   equations (*e.g.,*[16-19]). The LBM is based on Boltzmann's equation [20], which was derived

151   from the gas kinetic theory. In this method, streaming and collision operator are employed to

152   describe the time and spatial evolution of a distribution function of particles. Boltzmann's equation

153   has a direct relationship with the Navier–Stokes equations [21]. The LBM characterizes the fluid

154   at points located on a regular 2- or 3-dimensional lattice. For the present work, a so-called D3Q15

155   lattice is used, meaning each point in three dimensions is linked to neighboring points through

156   fifteen velocity vectors e_0 to e_{14}, as shown in Figure 1.

157

158   *Figure. 1. D3Q15 lattice velocities.*

159

160   *2.2.1 Density distribution functions and their time evolution*

161   Each velocity vector, e_0 to e_{14}, has a corresponding density distribution function f_0 to f_{14}.

162   The density functions represent portions of a local mass density moving into neighboring cells in

163   the directions of corresponding discrete velocities. The macroscopic fluid density ρ at each lattice

164   point is a sum of the distribution functions at that lattice point:

$$\rho = \sum_{i=0}^{14} f_i \tag{11}$$

165   Fluid velocity at the lattice point is a weighted sum of lattice velocities, with distribution

166   functions being the weight coefficients:

167

$$\boldsymbol{u} = \frac{\sum_{i=0}^{14} f_i \boldsymbol{e}_i}{\sum_{i=0}^{14} f_i} = \frac{\sum_{i=0}^{14} f_i \boldsymbol{e}_i}{\rho} \tag{12}$$

168   where f_i/ρ ratio can be interpreted as a probability of finding a particle at a given spatial location

169   with a discrete velocity $\boldsymbol{e}_i$.

170   The model is completed by defining a collision operator that defines the evolution of the

171   density distribution. Using the collision model of Bhatnagar-Gross-Krook (BGK, [22]) with a

172   single relaxation time, the time evolution of the distribution functions is given by

$$f_i(\boldsymbol{r} + \boldsymbol{e}_i \Delta t, t + \Delta t) = f_i(\boldsymbol{r}, t) + \frac{1}{\tau_u}\left(f_i^{eq}(\boldsymbol{r}, t) - f_i(\boldsymbol{r}, t)\right), i = 0 \dots 14 \tag{13}$$

173   where $\boldsymbol{r}$ and t are the space and time position of a lattice site, Δt is the time step, and τ_u is the

174   relaxation parameter for the fluid flow. The relaxation parameter τ_u specifies how fast each density

175   distribution function f_i approaches its equilibrium f_i^{eq}. Kinematic viscosity, v, is related to the

176   relaxation parameter, τ_u, the lattice spacing, Δx, and the simulation time step, Δt, by

$$v = \frac{\tau_u - 0.5}{3} \frac{\Delta x^2}{\Delta t} \tag{14}$$

177   Depending on whether the model is two- or three-dimensional and given a particular set of

178   the discrete velocities $\boldsymbol{e}_i$, the corresponding equilibrium density distribution function can be found

179   [23]. For the D3Q15 lattice, the equilibrium distribution functions f_i^{eq} are

180

$$f_i^{eq}(\boldsymbol{r}) = \omega_i \rho(\boldsymbol{r}) \left(1 + 3 \frac{\boldsymbol{e}_i \cdot \boldsymbol{u}(\boldsymbol{r})}{c^2} + \frac{\frac{9}{2}(\boldsymbol{e}_i \cdot \boldsymbol{u}(\boldsymbol{r}))^2}{c^4} - \frac{\frac{3}{2}\boldsymbol{u}(\boldsymbol{r}) \cdot \boldsymbol{u}(\boldsymbol{r})}{c^2} \right) \tag{15}$$

181   with the lattice velocity $c = \Delta x / \Delta t$ and the weights

182

$$w_i = \begin{cases} \dfrac{2}{9} & i = 0 \\[2mm] \dfrac{1}{9} & i = 1 \dots 6 \\[2mm] \dfrac{1}{72} & i = 7 \dots 14 \end{cases} \tag{16}$$

183

184   Using the Chapman-Enskog expansion [21], it can be shown that LBM Eqs. 11 to 13

185   provide an approximation of the incompressible Navier-Stokes. The Navier-Stokes equations are:

186

$$\rho \left[\frac{\partial \boldsymbol{u}}{\partial t} + \boldsymbol{u} \cdot \nabla \boldsymbol{u} \right] = \nabla \cdot (\mu \nabla \boldsymbol{u}) \tag{17}$$

$$\nabla \cdot \boldsymbol{u} = 0 \tag{18}$$

187

188   where the $\mu = \nu \rho$ is the dynamic viscosity of fluid. The approximation is valid in the limit of low

189   Mach number $M = |\boldsymbol{u}| / c_s$, with a compressibility error in Eq. 18 on the order of $\sim M^2$ [17], where the

190   lattice speed of sound is $c_s = c/\sqrt{3}$. Note that the fluid compressibility used to control pore pressure

191   response is actually considered an error in general LBM applications. The fluid compressibility

192   can be calculated as:

$$\beta = \frac{1}{\rho c_s^2} \tag{19}$$

193   where ρ is the fluid density and c_s is the lattice speed of sound.

194

195   *2.2.2 Immersed moving boundary*

196   The immersed moving boundary (IMB) technique [24-26] allows solid boundaries to move

197   through the LBM computational grid. The IMB method introduces a subgrid resolution at the solid-

198   liquid boundaries, resulting in smoothly changing forces and torques exerted by the fluid on

199   moving particles. The IMB introduces an additional collision operator Ω_i^S expressing collisions of

200   solid particles with fluid as

$$\Omega_i^S = f_{-i}(\boldsymbol{r}, t) - f_i(\boldsymbol{r}, t) + f_i^{eq}(\rho, \boldsymbol{U_S}) - f_{-i}^{eq}(\rho, \boldsymbol{u}) \tag{20}$$

where U_S is the rigid body velocity of the particle that includes rotational and translational

velocities.

201

202   The time evolution of the density distribution functions in IMB now includes Ω_i^S

$$f_i(\boldsymbol{r} + \boldsymbol{e}_i \Delta t, t + \Delta t) = f_i(\boldsymbol{r}, t) + [1 - \beta(\epsilon, \tau)]\frac{1}{\tau}\left(f_i^{eq}(\boldsymbol{r}, t) - f_i(\boldsymbol{r}, t)\right) + \beta(\epsilon, \tau)\Omega_i^S \tag{21}$$

203   where the weighting factor $\beta(\epsilon,\tau)$ depends on solid coverage ϵ and relaxation parameter τ

$$\beta(\epsilon, \tau) = \frac{\epsilon}{1 + \dfrac{1 - \epsilon}{\tau - 0.5}} \tag{22}$$

204   Multiple values for $\beta(\epsilon,\tau)$ exist, but the value chosen in Equation 22 was used from [25].

205   *2.2.3 Fluid force and torque*

206   The total hydrodynamic force exerted by the fluid on a particle is calculated by summing

207   the momentum change at every lattice cell due to the new collision operator:

$$F_F = \sum_n \left(\beta_n \sum_{i=0}^{14} \Omega_i^S e_i \right) \tag{23}$$

208   The total hydrodynamic torque can then be calculated by:

$$T_F = \sum_n (r_n - r_c) \times \left(\beta_n \sum_{i=0}^{14} \Omega_i^S e_i \right) \tag{24}$$

209   where r_{n-r_c} is the vector from the center of the particle to the center of the lattice cell. Equations

210   23 and 24 appear in lattice units and need to be multiplied by $\Delta x^3 / \Delta t$ to convert to physical units.

211   It should also be noted that the IMB does not resolve detailed particle-fluid interactions such as

212   lubrication forces although the contact radius of the DEM is usually large enough to minimize

213   nodal conflicts [25].

214   *2.2.4 Boundary Conditions*

215   The corners created by intersecting platens represent the intersection of two independently

216   moving boundaries that requires special treatment. To resolve the no slip boundary conditions in

217   the corners of the domain, the values for the distribution functions were explicitly stated for lattice

218   points at the corner of two or more walls. Zou and He [27] proposed a method to solve for the

219   unknown distribution functions for these boundary nodes. Ho *et al*. [28] derived these equations

220   for both 2D and 3D lattices for certain wall configurations. By applying this boundary condition

221   explicitly at the corners, the fluid boundary conditions at the corners were consistent. To determine

222   the force exerted on the boundaries, the stress tensor was integrated over the area of the boundaries

223   [29].

224   ***2.3 Coupled DEM-LBM***

225   For coupling the DEM and the LBM, the LBM calculates the forces exerted on the solid

226   boundary by the fluid and passes the information to the DEM. Then, the DEM uses the total force

227   on the solid boundary to integrate the equations of motion for the solid particles. To visualize the

228   coupling of the DEM and LBM, a screenshot was taken from a sedimentation simulation with the

229   contributions from each method highlighted in Figure 2. The example of sedimentation illustrates

230   the dominant effects of each component of the coupled system. For example, in the region where

231   the particles are settling, the DEM inter-particle forces dominate the fluid forces, resulting in the

232   particle stacking shown in the left insert. However, in the fluid mixing region shown in the right

233   insert, the LBM fluid forces control the motion of the particles.

234   The LBM time step Δt is determined from the kinematic viscosity of fluid v, required grid

235   resolution Δx, and constraints on the relaxation parameter ($\tau > 0.5$) according to Eq. 14. The

236   relaxation parameter must be chosen low enough to achieve a sufficient time resolution. An upper

237   limit on the relaxation parameter is given by the low Mach number constraint. For DEM, the largest

238   stable time step value is estimated from the smallest particle mass m_i and the stiffest spring k_i in

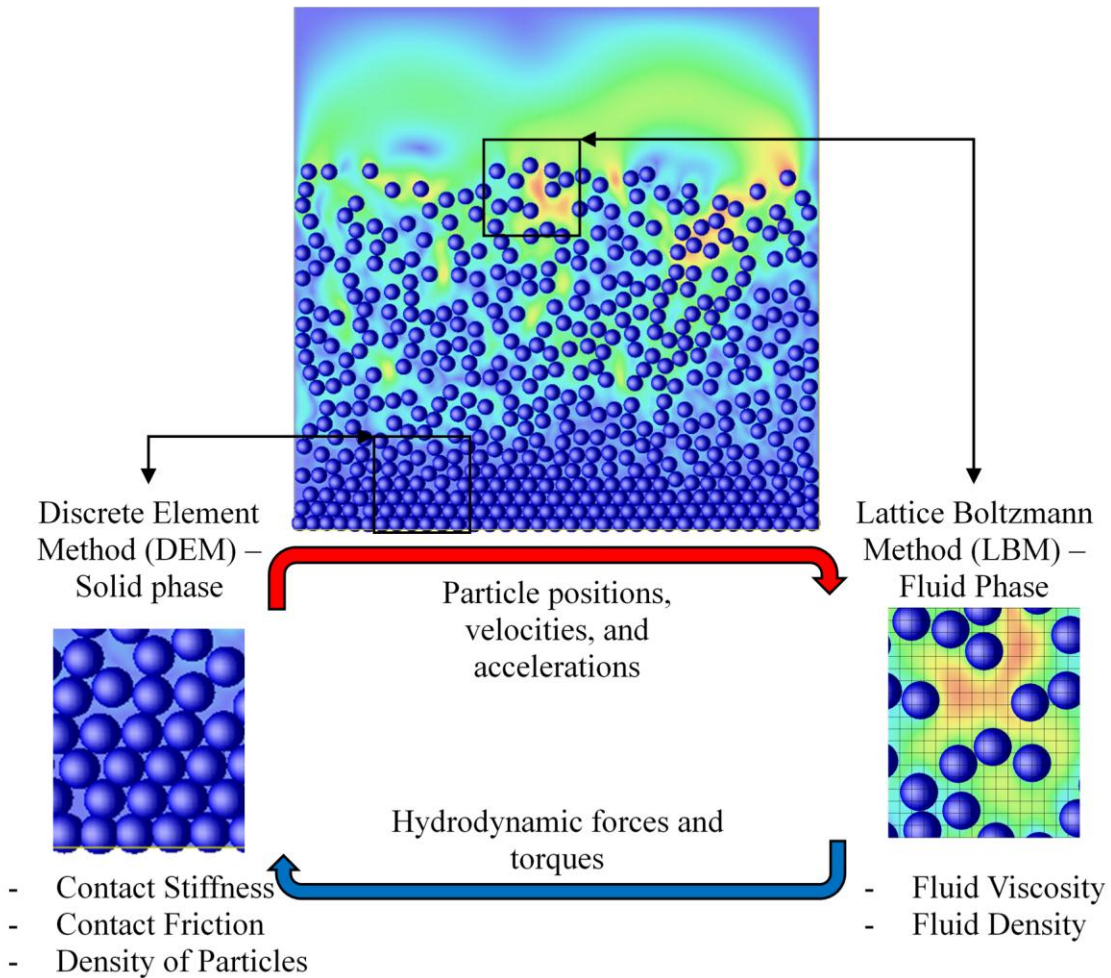239   the system, given the frequency of fastest oscillations

$$\omega_{max} = \sqrt{\frac{Max(k_i)}{Min(m_i)}} \tag{25}$$

240   and their time period

$$T_{min} = \frac{2\pi}{\omega_{max}} \tag{26}$$

241   In this work, the LBM time step is constrained to be greater than or equal to the DEM time

242   step. Accordingly, the LBM time step is determined first, and then the DEM time step is adjusted

243   to perform an integer number of substeps before performing the LBM calculation. To couple the

244   two methods, the DEM first calculates contact forces and torques between the particles. The LBM

245   then receives locations and velocities of the particles and solves the fluid equations. The LBM

246   calculates the fluid forces and torques on the particles at the current positions and adds those forces

247 and torques to the DEM's contact forces and torques. Finally, the DEM integrates the equations of

248 motion and updates the locations and velocities of the particles. During the DEM subcycling, the

249 fluid forces and torques remain constant, and the fluid-solid boundary does not move. Therefore,

250 care must be taken when deciding the number of DEM subcylces [26].

251

252 *Figure 2. Diagram showing the coupling of the DEM and LBM. In the LBM (Fluid Phase)*
253 *image, each square represents a 5x5 lattice grid demonstrating how the lattice size compares to*
254 *particle size.*

255

256   The presented DEM-LBM simulations were performed on the Shadow cluster at the

257 Mississippi State University High Performance Computing Collaboratory. The research code used

258 in this study was developed as a collaboration between Mississippi State University and the US
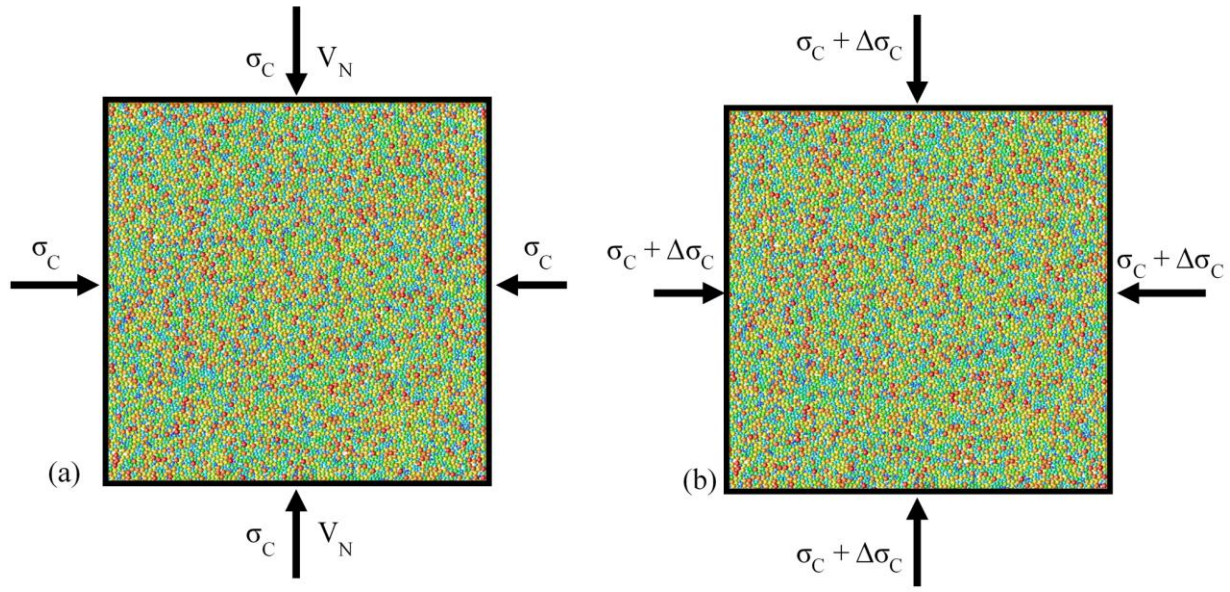
14

259   Army Engineer Research and Development Center. The LBM portion of the algorithm was

260   parallelized using spatial domain decomposition algorithm, as described in [15].

261   **3. Model Setup and Input Parameters**

262   To investigate the ability of the LBM to properly impose the undrained constraint, a two-

263   dimensional biaxial test is simulated using the coupled DEM-LBM model as well as a DEM-only

264   constant volume (DEM-CV) model. The focus in this paper is on the biaxial test, which involves

265   highly confined loading of dense particle systems that display significant dilation. The biaxial

266   DEM-only simulation is especially well suited as a reference for the present DEM-LBM

267   investigation because in the reference simulation, the boundary displacements were imposed to

268   maintain the constant domain volume, thus approximating the undrained condition in absence of

269   a fluid phase. In systems such as the biaxial test, the compressibility of the fluid phase is critical

270   to achieving realistic undrained conditions. The incompressibility condition is only approximated

271   in the LBM and is tied to the simulation time step and grid spacing. The issue investigated in this

272   study is whether the LBM compressibility is sufficiently small to represent the undrained loading

273   with specific fluid compressibility. The following sections show that the LBM can effectively

274   model realistic fluid behavior. The biaxial test requires a simple computational domain that is

275   easily discretized by the LBM grid and in which the undrained condition can be simulated either

276   by coupling the DEM to the LBM or by applying displacement boundary condition. The idealized

277   boundary conditions imposed by eliminating volume change through the boundary displacement

278   represent the benchmark against which the efficacy of the LBM model of the fluid phase is

279   assessed.

280   To model the biaxial specimen, 9409 particles with radii between 0.71 μm and 1.42 μm

281   were loosely placed inside the DEM-only domain. This placement was followed by a compressive

282   consolidation with external stress applied equally to all four-boundary walls. The final dimensions

283   of the walls were 101.5 μm x 101.5 μm. After reaching equilibrium under the desired confining

284   stress, the LBM fluid was introduced into the calculation, and the boundary conditions shown in

285   Figure 3 were imposed. Note that in Figure 3, the boundary stress condition is actually a force-

286   controlled displacement condition applied though rigid walls; the force applied to the wall is the

287   average stress component perpendicular to the wall times the contact area. To use the 3D LBM

288   with D3Q15 lattice shown in Figure 1, a periodic boundary condition was used in the in plane (z)

289   direction with enough spacing to minimize in-plane stresses. The spherical particles are embedded

290   in the LBM grid giving a 3D geometrical configuration that creates flow paths around the spheres.

291   Therefore, the fluid regime is three-dimensional. However, given that particle centers are aligned

292   along the x-y plane, the fluid force in the z-direction is negligible and does not create any particle

293   instability. No-slip boundary conditions were applied for the fluid velocities at the walls. For the

294   biaxial test, the vertical walls have an imposed velocity, and the velocity of the horizontal wall is

295   determined by the interaction of the fluid and particle stresses on the wall. For the B-value test, an

296   external stress is applied to each wall, and the resulting velocity of the wall is governed by the total

297   stresses of the system.

16

Figure 3. Boundary conditions and particle configurations for the a) Biaxial Test and b) B-value Test where σ_c is a compressive stress and V_N is a normal velocity. Note that periodic boundary conditions were used in the z-direction.

At the shearing stage of the biaxial test, the initial confining stress is applied to all four walls while a displacement boundary condition is applied to the top and bottom boundaries via a normal velocity V_N. Once the top and bottom walls start moving, the fluid resists volume decrease by exerting stress on the left and right boundaries. For comparison purposes, the DEM-CV simulation was also performed in which the left and right boundaries were displaced at a rate that maintained a constant domain volume in a manner similar to Peters and Walizer [11].

The initial particle configuration for this work was taken from Peters and Walizer [11] effort that investigated dilative material under constant-volume conditions in a biaxial test configuration. The large domain size in the referenced work resulted in stability problems when choosing appropriate parameters for the LBM. To keep the Reynolds number low, the system size from [11] was scaled down and a set of parameters from Table 1 was applied. The DEM simulations exhibits a dimensionless behavior with respect to the particle and domain sizes.

17

315 Coupled simulations were performed for varying LBM grid sizes, with the grid spacing set to at

316 least 6 LBM cells per particle. Also, the rigid walls are assumed to be frictionless so that the forces

317 between the particles and walls are purely normal forces [11].

318

319 *Table 1. Model parameters used for the smaller particle simulations.*

Property	Units	Value
Maximum diameter	μm	1.42
Minimum diameter	μm	0.71
Normal stiffness	N/m	1.43E-2
Shear stiffness	N/m	2.86E-3
Coefficient of restitution	---	0.1
Contact friction	---	0.5
Initial height	μm	101.5
Initial width	μm	101.5
Initial porosity	---	0.15
Fluid viscosity	Pa-s	0.00112
Fluid density	kg/m^3	1000.0
Grid spacing	μm	0.123

320

4. Results

321 **4. Results**

322 To better understand the effects of the LBM compressibility on the biaxial simulation,

323 Skempton's pore pressure parameter B was first simulated and then computed for the coupled

324 DEM-LBM system. The DEM-LBM model of the biaxial test was then used to investigate the

18

325   effects of fluid compressibility and particles size. For each case, the results were compared against

326   those attained from the DEM-CV model. The results are presented and discussed in the following

327   sections. The effective stress path invariants are used to represent the stress history of the system

328   for the biaxial case:

$$p' = \frac{\sigma_1 + \sigma_2}{2} \tag{27}$$
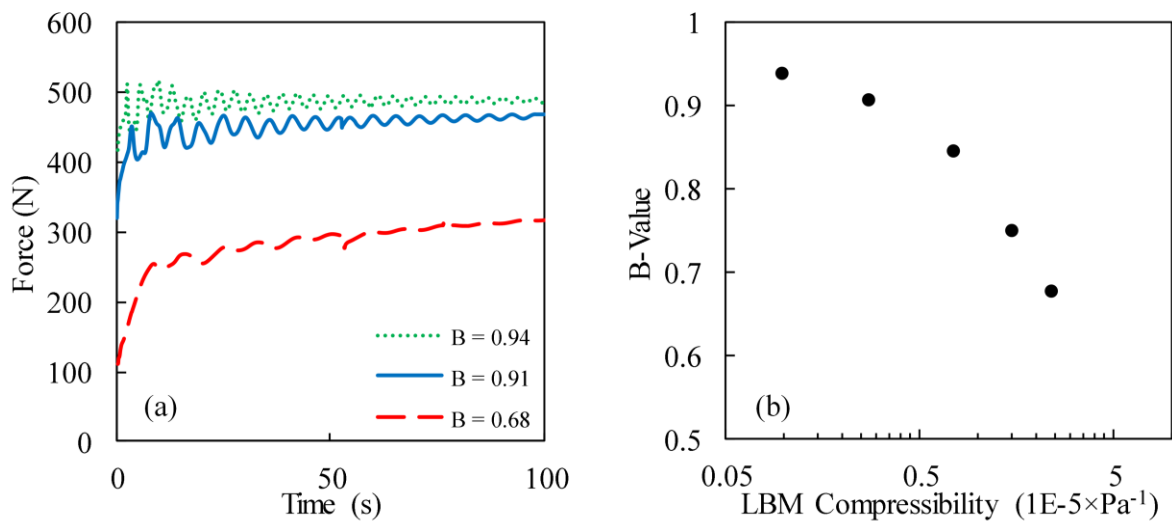
$$q = \frac{\sigma_1 - \sigma_2}{2} \tag{28}$$

329   where σ_1 is the most-compressive principal stress and σ_2 is the least-compressive principal stress.

4.1. B-value Test

331   Skempton's pore pressure parameter B is an important property that describes the pore

332   pressure response in an undrained porous medium under changes in total stresses. The B-value

333   test is a type of compression test where the response of the fluid can be evaluated. The test is used

334   in laboratory to assess saturation of a specimen before shearing it. Theoretically, the B-value is

335   defined to be the ratio of the induced pore pressure increment to the change in total hydrostatic

336   stress increment for undrained conditions [30]. In this study, the B-value test was numerically

337   simulated by applying an equal confining stress to all walls around the initial particle domain,

338   including the LBM fluid, as shown in Figure 3b. These applied stresses are total stresses. The

339   average hydrodynamic stress was computed by integrating the values of fluid pressure at the walls.

340   The B-value was determined as the ratio of the averaged hydrodynamic stress to the applied total

341   stress. The B-value test was performed for different values of LBM compressibility, as calculated

342   by Eq. 19, to understand the convergence of the LBM pressure response with respect to lattice

343   compressibility. The compressibility of the LBM fluid was varied by keeping the grid spacing and

344   fluid viscosity constant while changing the time step and the lattice relaxation parameter. The

345   simulated time for *B*-value tests was chosen long enough for the forces exerted on the boundaries

346   to reach a steady state value.

347   To calculate the *B*-value of the DEM-LBM system, the average hydrodynamic stress

348   exerted on the four boundaries was determined. The forces exerted on the walls initially oscillate,

349   but after a long enough simulation time, the oscillations settle to a steady state value as shown in

350   Figure 4a. As expected, by decreasing the LBM compressibility, the *B*-value approaches the value

351   of unity as seen in Figure 4b. A theoretical *B*-value was calculated by determining the soil's

352   compressibility under the same loading conditions except without the fluid. The obtained value

353   was then used with the LBM compressibility to determine a theoretical *B*-value. The results for

354   this comparison are shown in Table 2.

355

356   *Figure 4. Results from the B-value test. a) Average hydrodynamic forces on the confining walls.*
357   *b) B-value versus LBM compressibility showing the convergence of the B-value for the system.*
358

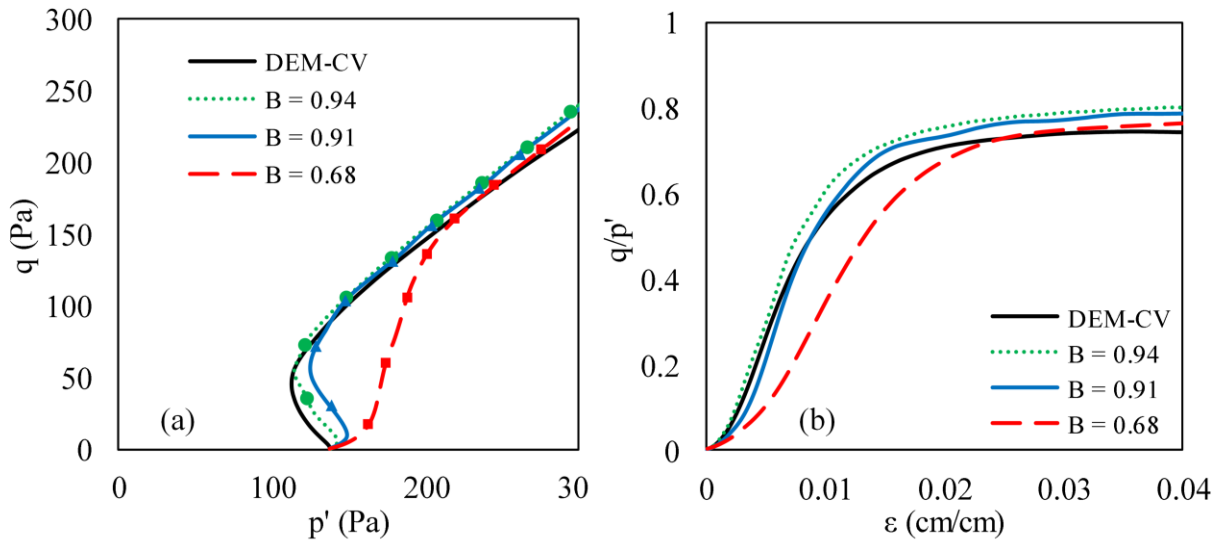359   *Table 2. Comparison of the DEM-LBM and a theoretical B-value.*

Fluid Compressibility (1/Pa)	DEM-LBM B-value	Theoretical B-value
9.65E-7	0.94	0.998

2.70E-6	0.91	0.994
7.39E-6	0.85	0.982
1.50E-5	0.75	0.965
2.40E-5	0.68	0.946

360

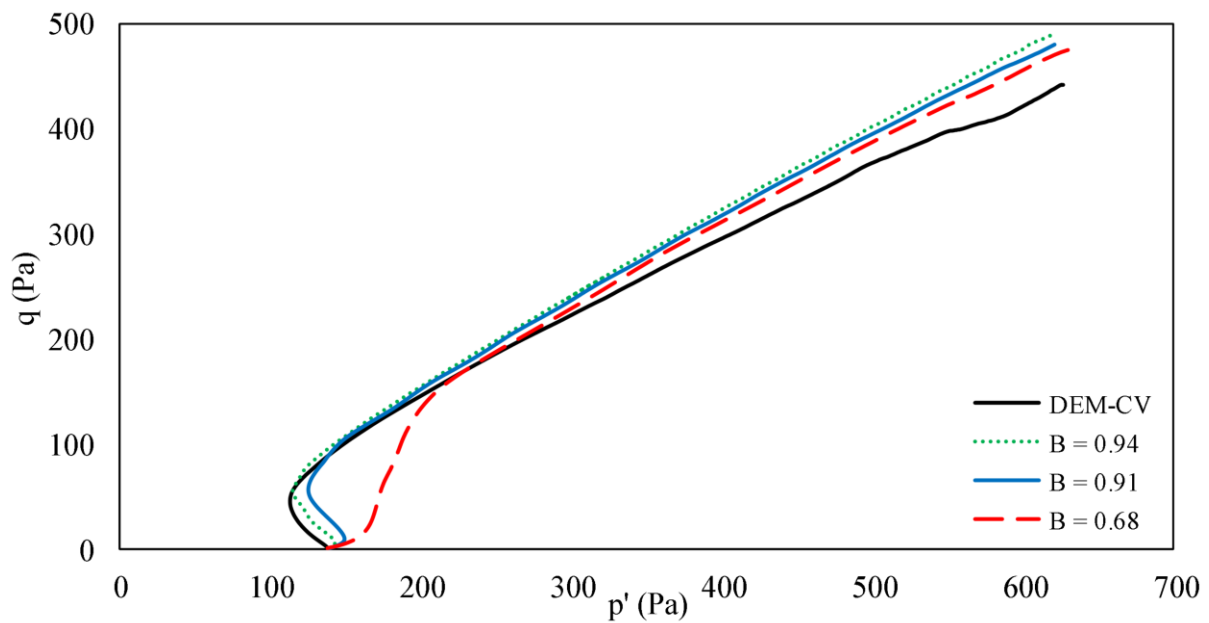### 4.2. Effects of Fluid Compressibility in Biaxial Simulation

362   The stress paths and stress ratio versus strain plots for the simulations are shown in Figure

363   5a. The plots are annotated with the DEM-LBM B-values from Table 2. Two main regions were

364   of interest for the biaxial simulation. At the strain values lower than 4% the stress path and the

365   stress ratio for the DEM-LBM system had a strong dependence on the B-value of the system. As

366   expected, for lower values of B, the system behaved more like a drained system. By decreasing

367   the LBM compressibility, thus increasing the B-value, the DEM-LBM converged to the values

368   generated by the DEM-CV model. Figure 5 depicts the importance of imposing a large enough B-

369   value to capture the initial behavior of the system.

370

371   *Figure 5. a) Stress path plot for low values of strain (4%) showing the effects of LBM*
372   *compressibility. Note that each marker represents 0.5% increments of strain. b) Stress ratio*
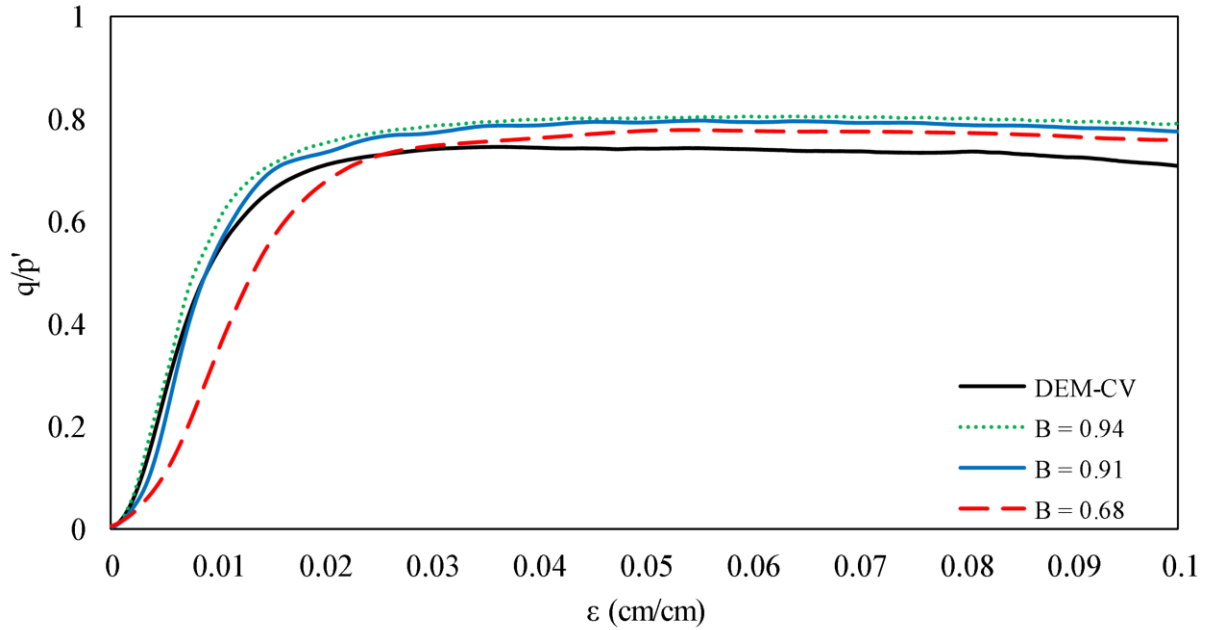373   *versus strain plot for the first 4% of strain.*
374

375   After reaching 4% of strain, the DEM-LBM showed slightly larger values of stress than

376   the DEM-CV model. Although the stresses for small values of stress differ greatly depending on

377   the *B*-value, the DEM-LBM model shows relatively good agreement after 4% strain for varying

378   values of *B* as shown in Figures 6 and 7.

379

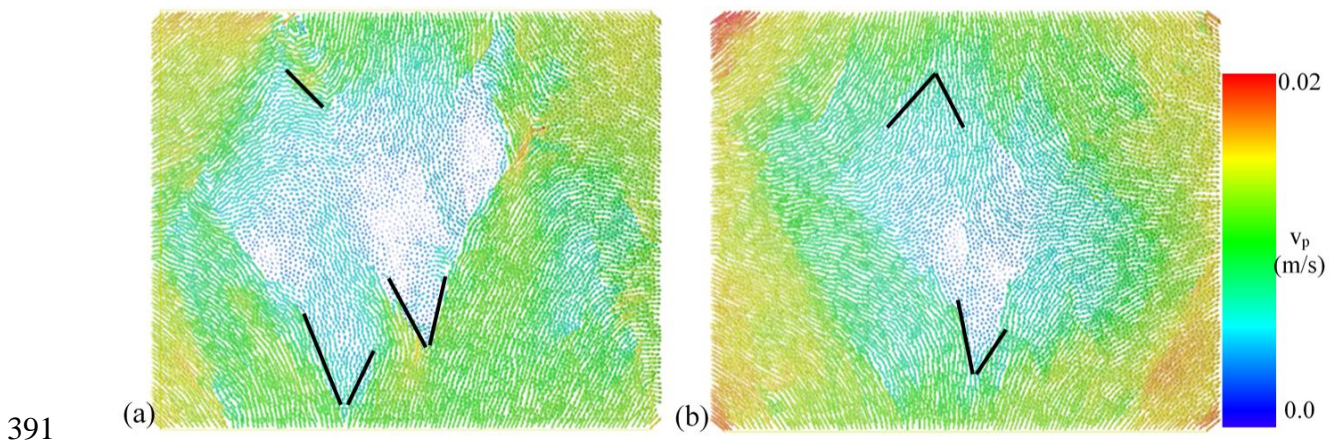380   *Figure 6. Stress path plot for the full simulation at 3 different B-values.*
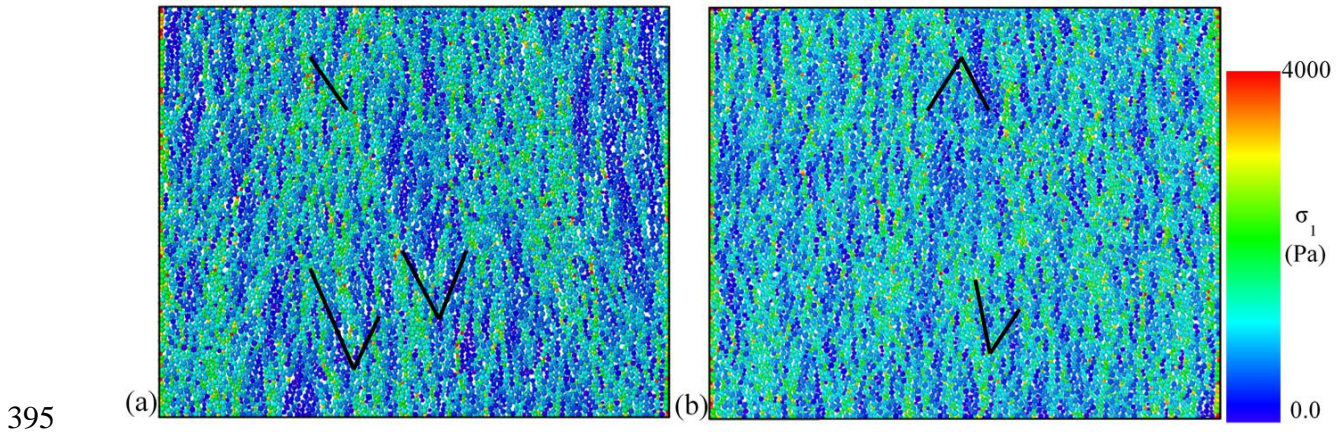381

382

Figure 7. Stress ratio plots for the full simulation.

384   To analyze the differences in the stress values between the DEM-CV and DEM-LBM

385   models for larger strain, plots for vectors of the velocity field and interparticle stresses were

386   generated, as seen in Figures 8 and 9. When comparing the results of these plots, the shearing

387   zones from the DEM-CV model are better delineated and more abundant than those from the

388   DEM-LBM model, possibly explaining differences in the stress paths. Shear band formation was

389   identified as linear regions where there are discontinuities in particle velocities. These regions are

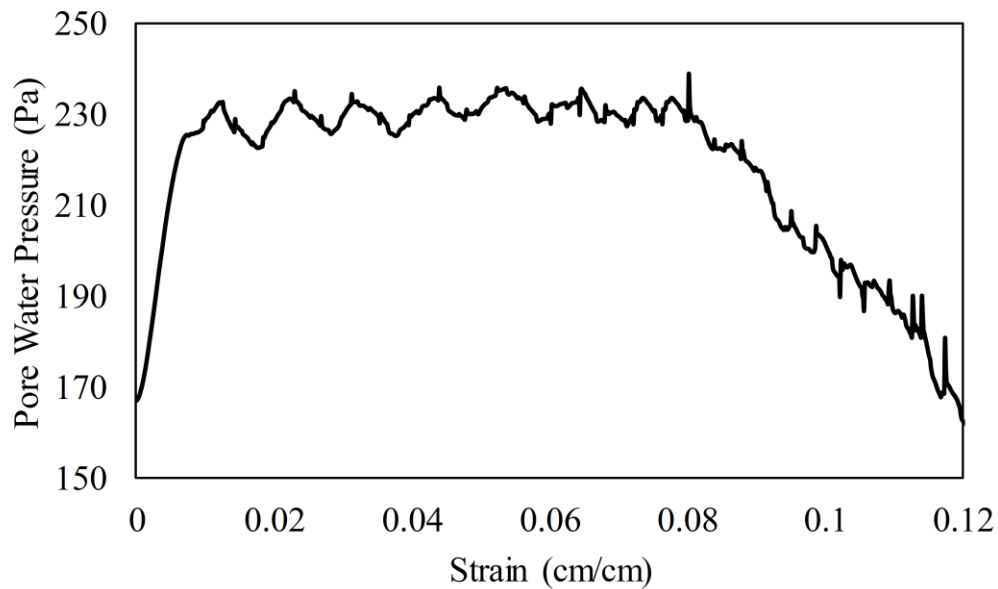390   delineated by black lines shown in Figure 8.

391   (a)   (b)

392   *Figure 8. Velocity vector for the particles at 10% strain for a) DEM-CV and b) DEM-LBM. The*
393   *solid black lines shown in the figure represent the locations of shear bands.*
394

395   (a)   (b)

396   *Figure 9. Interparticle stress at 10% strain for a)DEM-CV and b) DEM-LBM. The solid black*
397   *lines shown in the figure represent the locations of shear bands.*
398

399   The pore water pressure is plotted in Figure 10. The plotted values represent the average

400   fluid pressure in the system. The initial pore pressure is approximately 170 Pa.

401

402

403   Figure 10. Average pore water pressure versus strain. Note the initial pressure of the system is
404   about 170 Pa.

405

5. Discussion

The most interesting and important result from the simulations is the effect of the fluid's compressibility on how well the model conserves volume and follows the correct stress path. The role of the fluid's compressibility can clearly be seen in Figure 5, where decreasing the fluid's compressibility allows the system to better match the DEM only undrained simulation. Another interesting discovery is that the *B*-value corresponding to the LBM's compressibility is much lower than the theoretical *B*-value for the respective compressibility, as shown in Table 2.

The differences in the stress plots for the DEM-CV and the DEM-LBM at large strains can be attributed to the formation of shear bands. The formation of a shear band is accompanied by strain softening along the band, which affects the stress in the entire domain. The local nature of the constant-volume constraint appears to limit the distribution of shear localization. When the constant volume constraint is imposed at the boundaries, volume changes are possible within the domain. When volume is constrained locally, particle migration is limited. Since the DEM-CV conserves the volume globally by enforcing specific boundary conditions and the DEM-LBM conserves volume locally, the systems showed slightly different behavior. The DEM-CV simulation forms very distinct shear bands with higher intensity and abundance than the DEM-LBM. The DEM-LBM did show shear band formation in the simulation, but there were not as many shear bands formed. By studying Figures 8 and 9, the DEM-LBM model shows a more uniform distribution of the stress and deformation resulting in less locality and larger average stress values.

The study was performed using larger and smaller sized particles, showing the invariance of behavior with respect to problem dimensions. The size of the system greatly influenced the

428   appropriate fluid properties for the LBM, and the smaller particles resulted in more physically

429   realistic fluid properties. However, the general behavior of both systems was very similar and does

430   not seem to depend on the physical size or the specific fluid properties, but rather on the

431   dimensionless parameters such as *B*-value and Reynolds number. Of course, the dimensional

432   invariance is the result of having no-flow conditions on all boundaries. In application problems,

433   where drainage can occur, the particle dimensions would affect the apparent Darcy permeability

434   and greatly change the obtained response. The initial area of the stress path is dominated by the

435   LBM compressibility. The final portion of the stress path differs when compared to the DEM-CV

436   model, which can be attributed to the development of shear bands.

437   The main goal of this study was to show the capabilities of the coupled DEM-LBM model,

438   and how this model could effectively simulate a fluid undergoing a compressive load while

439   conserving volume and accurately calculating the stress path of the system. To the best of the

440   authors' knowledge, no other model has been used for this type of problem, and the DEM-LBM

441   shows a promising capability to solve other geomechanical problems of this nature.

442   **6. Summary and Conclusions**

443   The coupled DEM-LBM model allows explicit modeling of both the solid and the fluid

444   phases for the undrained biaxial test. The DEM-LBM model showed a convergence to the *B*-value

445   of unity for decreasing the LBM compressibility, although for intermediate values of

446   compressibility the pore pressure response deviated from values anticipated from Skempton's

447   theory. Using the constant volume DEM only simulation as a comparison, the DEM-LBM model

448   showed a good agreement for the undrained biaxial problem. Visualizing the interparticle stresses

449   and particle velocity vectors provided insight into the formation of shear bands and the differences

450   between the DEM-CV and DEM-LBM.

451   By verifying the DEM-LBM model with the DEM-CV simulation, this study presents a

452   multiphase model that can simulate both phases in the undrained biaxial test and help understand

453   the mechanisms that cause shear band formation. The present study shows that the DEM-LBM

454   model can accurately simulate a compressive/expansive loading on the outer boundaries. By doing

455   so, the DEM-LBM model shows a valuable capability for solving a multitude of similar

456   geomechanical problems, taking advantage of parallel supercomputers. Future work should

457   consider cases where fluid flow can occur at boundaries for which fluid permeability has a strong

458   influence on the pore pressure response.

464

References

1. Han Y, Cundall PA. LBM–DEM modeling of fluid–solid interaction in porous media. *International Journal for Numerical and Analytical Methods in Geomechanics* 2013; 37, no. 10: 1391-1407.

2. Lambe TW, Whitman RV. *Soil mechanics SI version*. John Wiley & Sons, 2008.

3. Cundall PA, Strack ODL. A discrete numerical model for granular assemblies. *Géotechnique* 1979; 29:47–65(18), doi:10.1680/geot.1979.29.1.47.

4. Soga K, Kumar K, Biscontin G, Kuo M. Geomechanics from Micro to Macro. *CRC Press*, 2014.

5. Alonso-Marroquın F, Vardoulakis I. Micromechanics of shear bands in granular media. *Powders and grains* 2005; 701–704.

6. Sun W, Kuhn MR, Rudnicki JW. A multiscale dem-lbm analysis on permeability evolutions inside a dilatant shear band. *Acta Geotechnica* 2013; 8(5):465–480.

7. Lominé F, Scholt`es L, Sibille L, Poullain P. Modeling of fluid–solid interaction in granular media with coupled lattice boltzmann/discrete element methods: application to piping erosion. *International Journal for Numerical and Analytical Methods in Geomechanics* 2013; 37(6):577–596.

8. Yang ZX, Wu Y Critical State for Anisotropic Granular Materials: A Discrete Element Perspective. *International Journal of Geomechanics* 2016; 04016054.

9. Yimsiri S, Soga K. DEM analysis of soil fabric effects on behaviour of sand. *Geotechnique* 2010; 60(6), 483–495.

10. Yang ZX, Yang J, Wang LZ. On the influence of interparticle friction and dilatancy in granular materials: A numerical analysis. *Granular Matter* 2012; 14(3), 433–447.

487   11. Peters J, Walizer L. Patterned nonaffine motion in granular media. *Journal of Engineering*

488   *Mechanics* 2013; 139(10):1479–1490, doi:10.1061/(ASCE)EM.1943-7889.0000556

489   12. Tordesillas A, Pucilowski S, Walker DM, Peters JF, Walizer LE. Micromechanics of vortices

490   in granular media: connection to shear bands and implications for continuum modelling of

491   failure in geomaterials. *International Journal for Numerical and Analytical Methods in*

492   *Geomechanics* 2014.

493   13. Walker DM, Tordesillas A, Froyland G. Mesoscale and macroscale kinetic energy fluxes from

494   granular fabric evolution. Physical Review E 2014; 89(3):032 205.

495   14. Feng Y T, Han K, Owen DRJ. Combined three-dimensional lattice Boltzmann method and

496   discrete element method for modelling fluid-particle interactions with experimental

497   assessment. *International journal for numerical methods in engineering* 2010; 81.2: 229.

498   15. Jelinek B, Eshraghi M, Felicelli SD, Peters JF. Large-scale Parallel Lattice   Boltzmann   -

499   Cellular Automaton Model of Two-dimensional Dendritic Growth. *Computer Physics*

500   *Communications*. Elsevier 2013; *185*(3), 939-947.

501   16. Wolf-Gladrow DA. Lattice-Gas Cellular Automata and Lattice Boltzmann Models: An

502   Introduction. Lecture Notes in Mathematics, Springer, 2000, doi:10013/epic.14316.

503   17. Succi S. The lattice Boltzmann equation for fluid dynamics and beyond. Oxford University

504   Press: New York, 2001.

505   18. Rothman DH, Zaleski S. Lattice-Gas Cellular Automata: Simple Models of Complex

506   Hydrodynamics. Al´ea-Saclay, Cambridge University Press, 2004.

507   19. Sukop MC, Thorne DT. Lattice Boltzmann Modeling - An Introduction for Geoscientists and

508   Engineers. Springer: Berlin, 2006.

509   20. Boltzmann L. Weitere Studien über das Wärmegleichgewicht unter Gas-molekülen.

510   Wissenschaftliche Abhandlungen 1872; 1:316–402.

511   21. Chapman S, Cowling TG. The Mathematical Theory of Non-uniform Gases: An Account of

512   the Kinetic Theory of Viscosity, Thermal Conduction and Diffusion in Gases. Cambridge

513   University Press, 1970.

514   22. Bhatnagar PL, Gross EP, Krook M. A Model for Collision Processes in Gases. I. Small

515   Amplitude Processes in Charged and Neutral One-Component Systems. *Physical Review*

516   May 1954; 94:511–525, doi:10.1103/PhysRev.94. 511.

517   23. Qian YH, D'Humi´eres D, Lallemand P. Lattice BGK Models for Navier-Stokes Equation.

518   EPL (Europhysics Letters) 1992; 17(6):479, doi:10.1209/0295-5075/17/6/001.

519   24. Noble DR, Torczynski JR. A Lattice-Boltzmann Method for Partially Saturated Computational

520   Cells. *International   Journal   of   Modern   Physics   C*   1998;   9:1189–1201,

521   doi:10.1142/S0129183198001084.

522   25. Strack OE, Cook BK. Three-dimensional immersed boundary conditions for moving solids in

523   the lattice-Boltzmann method. *International Journal for Numerical Methods in Fluids*

524   2007; 55(2):103–125, doi:10.1002/fld.1437

525   26. Owen DRJ, Leonardi CR, Feng YT. An efficient framework for fluid–structure interaction

526   using the lattice Boltzmann method and immersed moving boundaries. *International*

527   *Journal   for   Numerical   Methods   in   Engineering*   2011;   87(1-5):66–95,

528   doi:10.1002/nme.2985.

529   27. Zou Q, He X. On pressure and velocity boundary conditions for the lattice Boltzmann BGK

530   model. *Physics of Fluids* 1997; 9(6):1591–1598, doi:10.1063/1.869307

531   28. Ho CF, Chang C, Lin KH, Lin CA. Consistent boundary conditions for 2D and 3D lattice

532   Boltzmann simulations. Computer Modeling in Engineering and Sciences (CMES) 44, no.

533   2 (2009): 137.

534   29. Mei R, Yu D, Shyy W, Luo LS. Force evaluation in the lattice Boltzmann method involving

535   curved geometry. *Physical Review E*. 2002;65(4):0412

536   30. Skempton AW. The pore-pressure coefficients A and B. *Geotechnique* 1954; 4(4), 143-147.

537